Available online at www.sciencedirect.com
SCIENCE DIRECT
Geochimica et Cosmochimica Acta 70 (2006) 3820–3829
Geochimica
www.elsevier.com/locate/gca

Relationship between solubility and solubility product: The roles of crystal sizes and crystallographic directions

Chunfang Fan [a], Jun Chen [b], Yang Chen [b], Junfeng Ji [b], H. Henry Teng [a,*]

[a] *Department of Chemistry, The George Washington University, Washington, DC 20006, USA*
[b] *Department of Earth Sciences, The Nanjing University, Nanjing, Jiangsu 210093, PR China*

Received 19 September 2005; accepted in revised form 6 June 2006

Abstract

Grain size- and crystallographic direction-dependence are among the fundamental characteristics of crystal solubility. However, such important material properties are routinely ignored and solubility is often conveniently approximated by a solubility product. In this study, we attempt to outline the relationship between solubility and solubility product using thermodynamic arguments, and to provide observations that demonstrate the occurrence of circumstances where the solubility product cannot properly approximate crystal solubility. Theoretical analysis shows that solubility is always greater than solubility product, but the difference is inversely related to the grain size. Furthermore, the difference can be crystallographic direction specific if the total surface energy change upon the attachment of an individual growth unit is nonequivalent for each symmetrically unrelated crystal faces. *In situ* AFM experiments conducted on the cleavage face of calcite demonstrate that the $\langle\bar{4}41\rangle\pm$ steps exhibit direction- and length-dependent behavior. Specifically, the measured critical step lengths are consistent with the predicted inverse relationship to saturation states. Moreover, step retreat at $\langle\bar{4}41\rangle_+$ and advance at $\langle\bar{4}41\rangle_-$ are observed simultaneously in a narrow range of saturation at near equilibrium conditions, indicating the existence of direction specific solubility. Whereas these findings justify the rationale for approximating solubility by solubility product in cases where large crystals are concerned, the results imply that the size and direction effect should not be ignored if nanocrystal growth/dissolution is the subject of interest.

1. Introduction

Solubility (K_b) is one of the critical parameters characterizing the behavior of crystallites in solution environments, yet K_b is also one of the material properties that we often take for granted from the textbook definition and thereby give little further thought to. Since the solubility relation was first proposed by Nernst more than a century ago (e.g. Nernst, 1889; Stieglitz, 1908), solubility product (K_{sp}) has become a synonym of solubility and K_{sp} has been used routinely to approximate K_b. However, with the advent of the Gibbs thermodynamic theory that delineates the controls of surface free energies on equilibrium constants (see the scientific papers of J. W. Gibbs, vol. I and the related review paper by Parks, 1990), it becomes clear that the chemical potential necessary to maintain the growth of an individual crystal differs for grains of different sizes and amongst faces that have different surface energies. This leads to the conclusion that solubility is dependent upon crystal size and crystallographic direction.

Whereas the size dependence of the solubility arises from the Gibbs–Thompson effect (Burton et al., 1951), the anisotropy in surface free energy results from the fact that the atomic structure of crystal faces can be very different in different crystallographic directions. Although not as well documented as the Gibbs–Thompson effect, direction specific surface free energies have been reported for a number of crystalline materials. For example, Smith and Hem (1972) found the surface free energies of the (001) and (100) faces of gibbsite to be 140 and 483 mJ/m^2, respectively. Che et al. (1998) calculated the surface free energies of molybdenum crystals and assigned values of

* Corresponding author.
E-mail address: hteng@gwu.edu (H.H. Teng).

0016-7037/$ - see front matter © 2006 Elsevier Inc. All rights reserved.
doi:10.1016/j.gca.2006.06.011

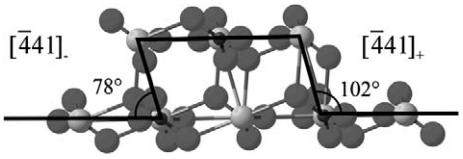

Fig. 1. Profile view of a monolayer $\{10\bar{1}4\}$ slice (~0.3 nm in thickness) showing the differences between the negative and the positive steps. Atoms of Ca, C, and O are represented by black (small), dark gray (large), and light gray circles (large), respectively.

3.34, 2.92, 3.24, and 3.11 J/m^2 for the (100), (110), (111), and (211) faces. Using molecular dynamics simulation, de Leeuw et al. (1999) obtained values of 0.35 and 0.68 J/m^2 for the positive and negative steps on calcite $\{10\bar{1}4\}$ faces. These findings suggest that direction specific solubility must exist. Yet, little evidence for this phenomenon can be found in the literature. This is because, under most circumstances, large crystals are under study and K_{sp} approximates K_b reasonably well. It is only when small (sub-micro to nanometric) crystals are involved that the size- and direction-dependence prove to be important, leading to significant deviations between the solubility product and the crystal solubility.

In the present study, we attempt to explore the $K_{sp} \sim K_b$ relationship and the dependence of K_b on grain size and crystallographic directions from equilibrium thermodynamic points of view. We then relate these theoretical considerations to experimental observations using calcite as an example. We do so by monitoring the morphology and movement of the $\langle\bar{4}41\rangle_+$ (positive) and $\langle\bar{4}41\rangle_-$ (negative) monomolecular steps (Fig. 1) under very near equilibrium conditions using *in situ* fluid cell atomic force microscopy (AFM). Currently, the available K_{sp} values (determined from the equilibrium compositions of the solutions containing calcite crystals during growth or dissolution) scatter from $10^{-8.30}$ to $10^{-8.58}$ (Jensen et al., 2002) and, hence, yield a fairly wide range for 'near equilibrium conditions'. In this study, we define 'very near equilibrium' as the saturation states where the $\langle\bar{4}41\rangle$ steps have no measurable motion. The purpose of this paper is to present theoretical arguments and experimental observations that demonstrate the occurrence of circumstances where solubility product cannot properly approximate crystal solubility.

2. Theoretical consideration

2.1. Dependence of K_b on crystal size

Following the classic Gibbs thermodynamic theory, a general solubility equation can be obtained through the following derivation. Consider the nucleation of a single crystal of any geometry with any number of faces that are not related by symmetry operations. At constant temperature and pressure, the free energy change upon the occurrence of the nucleation reaction in solution can be described by

$$dG = -\sum_i \nu_i \mu_i dn + \sum_j \gamma_j dA_j, \tag{1}$$

where G is the Gibbs free energy; μ_i is the chemical potential of the ith species in the liquid phase; ν_i is the stoichiometric coefficient of the ith species in the solid phase; n is the number of moles of solute involved in the reaction; and, γ_j and A_j are the surface free energy and the surface area of the jth type of faces, respectively. Using the definition of chemical potential,

$$\mu_i = \mu_i^\circ + RT \ln \alpha_i, \tag{2}$$

one can re-arrange Eq. (1) to show

$$\frac{dG}{dn} = -\sum_i \nu_i \mu_i^\circ - RT \ln \prod_i \alpha_i^{\nu_i} + \sum_j \gamma_j (dA_j/dn) \tag{3}$$

where μ_i° and α_i are the standard chemical potential and the activity of the ith species, respectively. At equilibrium, $dG/dn = 0$, $\sum_i \nu_i \mu_i^\circ = -RT \ln K^\circ$, and it then follows that the crystal solubility $K_b = \prod_i \alpha_i^{\nu_i}$ can be expressed as

$$\ln K_b = \ln K^\circ + \frac{1}{RT} \sum_j \gamma_j (dA_j/dn). \tag{4a}$$

This is the general definition of crystal solubility. Since the standard state equilibrium constant (K°) defines the solubility product (K_{sp}) of the solute compound, Eq. (4a) states that crystal solubility is always greater than the solubility product of the solute.

Re-writing Eq. (4a) using K_{sp}, volume (v) and density (ρ) of the crystal, and the molecular weight (W) of the solute compound, one obtains

$$\ln\ K_b = \ln K_{sp} + \frac{W/\rho}{RT} \sum_j \gamma_j (dA_j/dv). \tag{4b}$$

Given any characteristic dimension l of the crystal grain (e.g. diameter for spheres or side length for cubes), $\Sigma\gamma_j(dA_j/dv)$ can be approximated by $[\tau(2\bar{\gamma})/3l)]$ (Enüstün and Turkevich, 1960), leading to the simplification of Eq. (4b) to

$$\ln K_b = \ln K_{sp} + \frac{2\tau W/\rho}{3RT} (\bar{\gamma}/l), \tag{4c}$$

where τ is a geometrical factor of the nucleus (e.g. $\tau = 3$ for a sphere and $\tau = 6$ for a cube), $\bar{\gamma}$ is the mean surface free energy and can be regarded as the total surface energy divided by the total surface area of the crystal. Eq. (4c) is the same statement of the classic Gibbs–Thomson relationship, which predicts that solubility is size-dependent and that solubility product is invariant irrespective of crystallographic direction but can approximate solubility when the crystal grain is infinitely large. Rearranging Eq. (4c) into

$$K_b/K_{sp} = \exp(c/l), \tag{4d}$$

where $c = (2\tau W\bar{\gamma}/3\rho RT)$, one can clearly see the inverse relationship between (K_b/K_{sp}) and the grain size l.

2.2. Dependence of K_b on crystallographic directions

Consider the growth of a two-dimensional nucleus P× N with a diagonal symmetry plane that relates the two sets of non-equivalent steps P (for positive) and N (for negative) directions (Fig. 2). Confined by the symmetry, the P × N nucleus has three different types of corner sites: $C_{+,+}$ that separates the two P steps, $C_{-,-}$ that separates the two N steps, and $C_{+,-}$ that connects the P and the N steps. When steps advance, newly added surface area and related curvature (defined as the reciprocal of the radius of a corner) changes are associated exclusively with the corner sites. Following the approach by Teng et al. (1998), one can show that the free energy change resulting from the addition of a row of growth units at the P steps is

$$dG = -\sum_i \nu_i \mu_i dn_+ + (2\gamma_{+,-}dA_- + 2\gamma_{+,+}dA_+) \quad (5)$$

where n_+ is the number of moles of solute attached at the P edges, $\gamma_{+,-}$ and $\gamma_{+,+}$ are the surface free energies of the $C_{+,-}$ corner and the $C_{+,+}$ corner, respectively, and dA_- and dA_+ stand for the surface area increase at one side of the N and P edge, respectively. Rearranging Eq. (5) after substituting in the definition of chemical potential Eq. (2), we have

$$\frac{dG}{dn_+} = -\sum_i \nu_i \mu_i^\circ - RT\ln\prod_i \alpha_i^{\nu_i} + (2\gamma_{+,-}dA_- + 2\gamma_{+,+}dA_+)/dn_+. \quad (6)$$

Applying the same treatment as to Eq. (3), we show that the step specific solubility for the P edges is

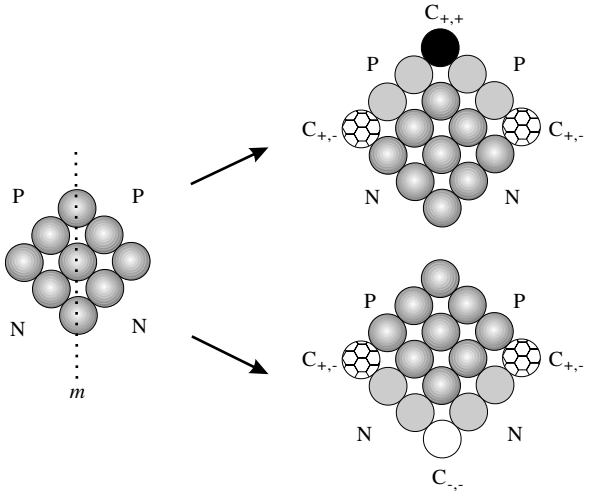

Fig. 2. Schematic representation of the growth processes of a two-dimensional nucleus P × N with a diagonal symmetry plane (m). Note that the newly formed surface area associated with the attachment of a row of growth units at step edges is limited to the $C_{+,+}$ (black circle) and the $C_{+,-}$ (hatched circles) corners for the P steps' advance (upper right), and the $C_{-,-}$ (open circle) and $C_{+,-}$ corners for the N steps' advance (low right).

$$\ln K_{b,P} = \ln K_{sp} + \frac{2}{RT}(\gamma_{+,-}dA_- + \gamma_{+,+}dA_+)/dn_+. \quad (7a)$$

A similar approach can yield the expression

$$\ln K_{b,N} = \ln K_{sp} + \frac{2}{RT}(\gamma_{+,-}dA_+ + \gamma_{-,-}dA_-)/dn_- \quad (7b)$$

that defines the step specific solubility for the N edges. A comparison of Eqs. (7a) and (7b) suggests that $K_{b,P}$ and $K_{b,N}$ will be different as long as the second terms on the right-hand side of the equations do not carry the same value, implying the occurrence of direction specific solubility on the same crystal.

Notice that, due to the same size effect described in Section 2.1, the second term in Eqs. (7a) and (7b) should decrease with increasing crystal size. This indicates that the direction specific solubility will converge at K_{sp} when crystals are infinitely large. This suggests that the direction dependence may not be important for growth and dissolution processes where larger (than a few micrometers) crystals are concerned.

3. Material and methods

3.1. Sample and solution preparation

Rhombohedral calcite fragments with a dimension of approximately $3 \times 2 \times 1$ mm^3 were cleaved from single crystals of optical-quality Iceland spar (Chihuahua, Mexico) with razor blades. The fragments were examined by optical microscopy to ensure that the cleavage faces were free of macro-steps and cracks. Each surface was then cleaned with a burst of N_2 (g) to remove any small adhering particles and mounted onto a glass cover using sealing wax. The glass cover was subsequently glued onto a steel puck. During the entire process of sample preparation, the calcite fragments were handled with tweezers to avoid surface contamination.

Experimental solutions were prepared by dissolving reagent grade sodium bicarbonate ($NaHCO_3$, Aldrich®, 99.99%+) and calcium chloride ($CaCl_2$, Aldrich®, 99.99%) into distilled, de-ionized water (DDW). Typical resistivity of the DDW is 18.2 MΩ-cm. A precision ultra-micro balance (PerkinElmer AD-6) with an accuracy of ±0.0000001 g was used to weigh out the reagents for solution preparation. The pH of the solutions (excluding the supersaturated solutions used to initiate spiral formation) was adjusted to 8.50 using a 0.999 N NaOH standard solution and measured by an Oakton 2500 pH meter that has an accuracy of ±0.01. The pH meter was calibrated by using three NIST-traceable buffer solutions of pH 4, 7, and 10. To minimize shifts in saturation state due to CO_2 degassing, solutions were sealed in volumetric flasks immediately upon completing preparation, and a new solution was made every 3–4 h during experimentation. Experimental solutions were injected into the fluid cell using a syringe pump. The total volume of the fluid cell was about 80 μl, and the available volume for fluid after discounting the

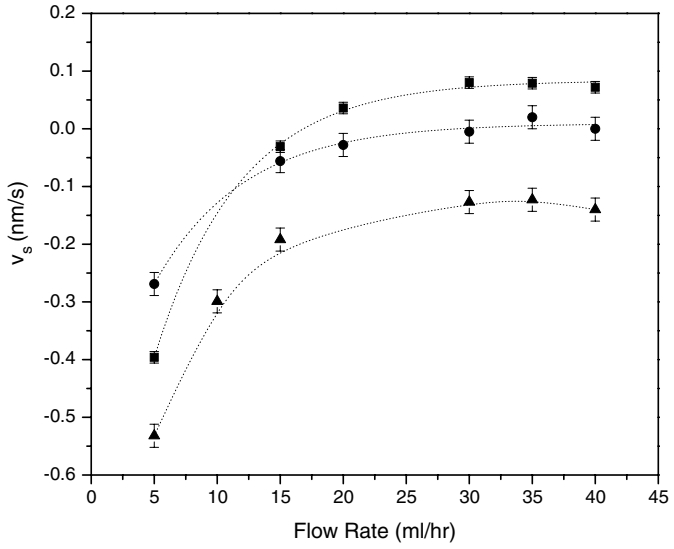

Fig. 3. Dependence of step velocity upon the flow rate of input solutions for *in situ* AFM measurements at near equilibrium conditions with $\Omega = \mathrm{IAP}/K_{sp} = 1.175$ (■), 1.023 (●), and 0.933 (▲). Note that when the flow rate is greater than 30 ml/h, the step velocity (approximated by the dashed lines to guide the eye) becomes independent of the flow rate regardless of saturation conditions.

space occupied by the AFM probe and seed crystal was on the order of 20 μl. To ensure that measured dissolution rates represented surface controlled dissolution processes and saturation states in the cell were as close to those of input solutions as possible, a flow rate of greater than 30 ml/h was used. This translates into a residence time of ~2.4 s for input solutions. Measurements from trial experiments showed that step speed at near equilibrium conditions became independent of flow rate above 30 ml/h (Fig. 3). All experiments were conducted at room temperature, but the temperature of each experimental solution in the fluid cell was measured *in situ* by a T type thermocouple probe connected to an Omega HH 506A thermometer with an accuracy of ±0.3 °C. The saturation state and chemical speciation in each solution at the experimental conditions were then calculated at the measured temperature using the numerical code MINTEQA2 (Allison et al., 1991). Depending upon the flow rate of the input solutions, the measured individual temperatures ranged from ~25 °C to ~37 °C. The overall errors (from reagent weighing and solution preparation, pH adjustment, and temperature measurement) in the computed saturation states were estimated to be ±2.64% on average.

3.2. Imaging by fluid contact AFM

In situ fluid cell imaging was conducted by a Nanoscope IIIa Scanning Probe Microscope (Digital Instruments) equipped with a J-type scanner (maximum scan area 120 × 120 μm) and commercially available oxide-sharpened Si_3N_4 probes. These probes consist of V-shaped cantilevers that have lengths of 100 and 200 μm and force constants of approximately 0.06–0.12 N/m. The square pyramidal shaped lever tips have a radius of approximately 4–50 nm. All images were captured in Contact Mode®.

Each experiment began on a newly prepared sample. The crystal surface was first scanned in air to ensure the quality of the imaging area. A supersaturated solution was subsequently injected to initiate growth; meanwhile growth hillocks with simple dislocation sources were located following methods described elsewhere (Teng et al., 1998, 2000). The growth hillocks were allowed to grow for 3–4 h at slight supersaturated conditions with minimal contact forces to reduce tip-induced surface damage (Park et al., 1996). Crystallographic orientation of the spirals was established by previously described methods (Teng et al., 1999). Once the growth hillocks became the dominant growth feature (i.e., without being outgrown by spirals with complex sources), experimental near-equilibrium solutions were injected to react with the surfaces. All images were collected at least 30 min after experimental solutions were introduced into the fluid cell.

3.3. Critical step length and step velocity measurement

Critical step lengths at different saturation states (defined by the saturation state $\Omega = \mathrm{IAP}/K_{sp}$ where IAP is the ionic activity product of Ca^{2+} and CO_3^{2-} in the solution) were measured as the lengths of the first steps developed on growth spirals at the moment step advance took place, following the methods given elsewhere (Land et al., 1997; Teng et al., 1998). Step velocities, v_{s-} and v_{s+} for the negative ($\langle\bar{4}41\rangle_-$) and the positive ($\langle\bar{4}41\rangle_+$) directions were determined by tracing the movement of individual points at steps relative to the y scan direction (Teng, 2005). This was achieved by first adjusting the scan angle so that the y-axis became parallel to the $\langle\bar{4}41\rangle_-$ and $\langle\bar{4}41\rangle_+$ steps, followed by disabling the slow direction scan to fix the position of the AFM tip. The values for v_{s-} and v_{s+} are given by the angles α and β (ref. to Fig. 1 in Teng et al., 2000) through

$$v_{s\pm} = \frac{S_r \times A}{N \times \tan\varpi} (\varpi = \alpha \text{ or } \beta), \quad (8)$$

where S_r and A are the scan rate (Hz) and the scan size, respectively, and N is the sampling rate (line/scan, 512 in this study). A value of 90° for α or β indicates still steps, whereas values greater or smaller than 90° represent advancing or retreating steps depending on the scan direction. In this study, the scan rates were set to range from 0.3 Hz to 1 Hz, corresponding to a capture time of approximately 28 to 9 minutes for each image. To minimize random errors in ϖ readings, only downward scans were used for the angle measurements.

4. Experimental observations

Upon the injection of supersaturated solutions into the fluid cell, growth hillocks with polygonized pyramidal

geometries were formed by the advancing monomolecular steps with a unit thickness of ~3.1 Å. These steps originated at dislocations that had a displacement vector (i.e. the Burgers vector) component intersecting the $\{10\bar{1}4\}$ crystal faces (Burton et al., 1951). The steps on the four flanks of the spirals were parallel to the $\langle\bar{4}41\rangle_+$ (i.e., $[\bar{4}41]_+/[48\bar{1}]_+$) and the $\langle\bar{4}41\rangle_-$ (i.e., $[\bar{4}41]_-/[48\bar{1}]_-$) directions, respectively. The step risers in the two sets of directions met the $\{10\bar{1}4\}$ cleavage surface at 102° and 78° (Paquette and Reeder, 1995), and will be referred to as positive and negative directions, respectively (Fig. 1). The two positive flanks were bisected by the *c*-glide plane and hence were crystallographically equivalent (ref. to Fig. 1 in Teng et al., 2000). The same was true for the negative flank pair but no symmetry operation relates the positive and the negative steps.

4.1. Saturation states vs. step lengths

Measurements of critical step lengths were collected at IAP $= 10^{-8.43}$, $10^{-8.39}$, $10^{-8.31}$, $10^{-8.25}$, $10^{-8.18}$, $10^{-8.09}$, $10^{-8.02}$, and $10^{-7.92}$. The corresponding saturation states (computed using the commonly cited value of $K_{sp} = 10^{-8.48}$, Plummer and Busenberg, 1982) are $\Omega = 1.12 \pm 0.03$, 1.23 ± 0.03, 1.48 ± 0.04, 1.69 ± 0.04, 1.99 ± 0.05, 2.45 ± 0.06, 2.88 ± 0.08, and 3.6 ± 0.1. The results of the measured critical step lengths against Ω are plotted in Fig. 4.

4.2. Saturation states vs. step directions

The behavior of approximately 1–2 μm long steps of growth spirals was monitored at different saturation conditions (i.e., IAP $= 10^{-8.41}$, $10^{-8.45}$, $10^{-8.47}$, and $10^{-8.51}$). Step advance was observed on all flanks of the spirals in solutions having IAP values greater than $10^{-8.41}$, with the positive steps advancing at a higher rate than the negative ones. However, as the IAP value approached $10^{-8.41}$, the $\langle\bar{4}41\rangle_+$ step edges became roughened, whereas the $\langle\bar{4}41\rangle_-$ steps remained smooth and straight (Fig. 5). A progressive decrease in IAP led to a reversal of the direction of step motion at the positive edges while the negative steps pursued their advance (Fig. 6). For example, average step velocity measured at IAP $= 10^{-8.45}$ were $v_{s-} = 0.02$ nm/s and $v_{s+} = -0.03$ nm/s for the negative and positive directions, respectively. Three replicate experiments revealed that the IAP value for the simultaneous occurrence of step advance and retreat on $\{10\bar{1}4\}$ faces ranges from $(10^{-8.41} \sim 10^{-8.45}) > \text{IAP} > 10^{-8.47}$. Step advance at the negative edges came to a halt at IAP $= 10^{-8.47}$ (Fig. 7) before detectable retreat was finally observed when solutions with an IAP value of $10^{-8.51}$ were introduced. At the latter saturation condition, steps on all flanks of the spiral hillocks retreated at mean $v_{s+} = -0.09$ and $v_{s-} = -0.05$ nm/s (Fig. 8).

5. Discussion

5.1. Possibilities for imaging distortion and impurity effect

Before concluding that the data presented above demonstrate that steps on calcite $\{10\bar{1}4\}$ faces have direction-dependent solubility, imaging artifacts and impurity effects on step behavior must be examined. A common problem in AFM imaging is the thermal drift of the piezoelectric

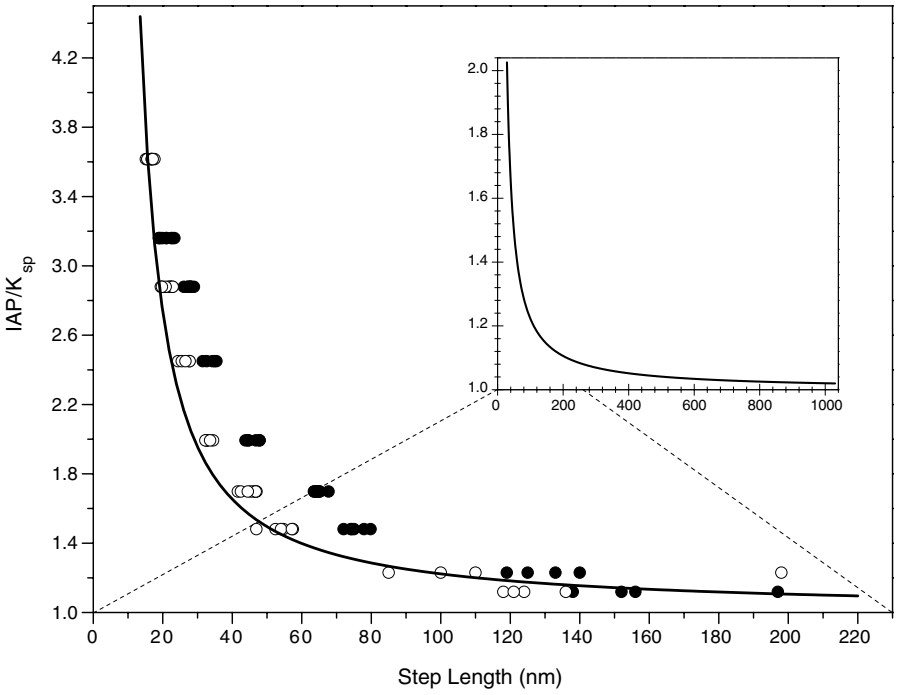

Fig. 4. Predicted (curve) and experimentally determined (solid circles, positive steps; open circles, negative steps) relationship between saturation state and critical step length in the $\langle\bar{4}41\rangle$ directions on calcite $\{10\bar{1}4\}$ faces.

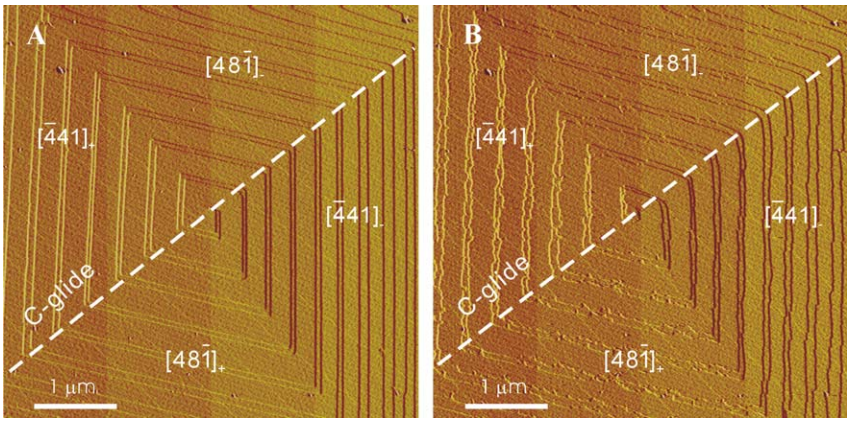

Fig. 5. Comparison of the $\langle\bar{4}41\rangle$ step morphologies (A) far from ($\Omega = 13$) and (B) near equilibrium (IAP $= 10^{-8.41}$). Notice that, while both the and $\langle\bar{4}41\rangle_+$ and $\langle\bar{4}41\rangle_-$ steps are straight and smooth at higher supersaturation conditions in (A), roughness develops in the $\langle\bar{4}41\rangle_+$ directions when the IAP approaches $10^{-8.41}$ in (B).

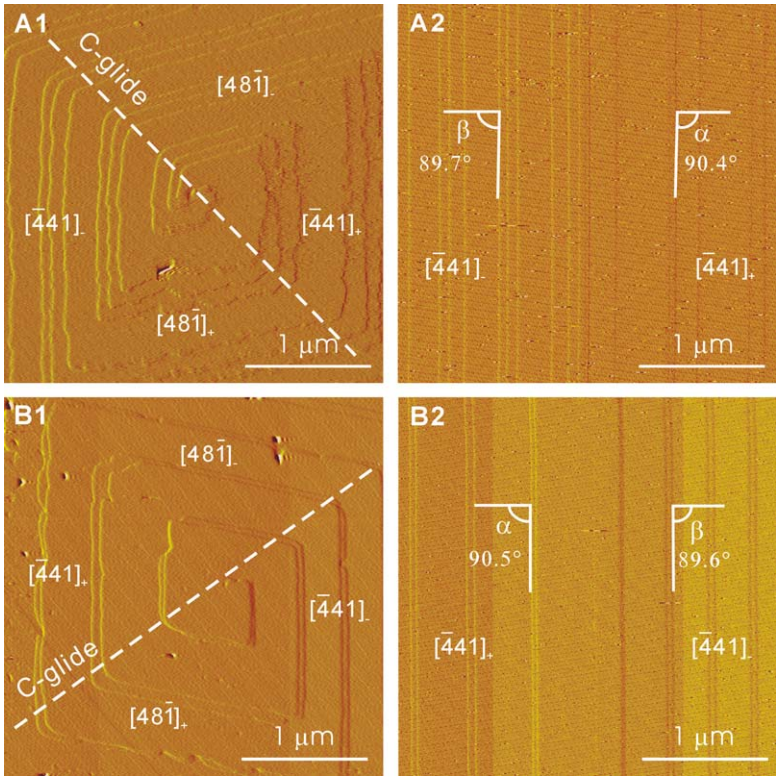

Fig. 6. Crystallographic direction specific behavior of the $\langle\bar{4}41\rangle_+$ and $\langle\bar{4}41\rangle_-$ steps in solutions with IAP $= 10^{-8.45}$ shown in AFM images with (A1 and B1) full scan and (A2 and B2) the slow scan axis disabled. Notice that $\alpha > 90°$ and $\beta < 90°$, indicating that the $\langle\bar{4}41\rangle_+$ and $\langle\bar{4}41\rangle_-$ steps are moving in different directions: one set of steps is dissolving while the other is growing.

scanner that causes the scanner to move away from the original field of view, changing the appearance of surface features in sequential images. In the present study, we measured the step motion on the same images by disabling the slow scan axis so that the AFM tips only raster in one dimension. By doing so, any imaging distortion should exert the same effect on the negative and positive steps since the AFM tips scan across the two steps at approximately the same time. Hence, the observed deviation of α or β from 90° on Figs. 5–8 should be mostly free of imaging artifacts.

It is well-documented that impurities can affect equilibrium solubility and growth/dissolution kinetics (e.g., Cabrera and Vermilyea, 1958; Simon and Boistelle, 1981; Voronkov and Rashkovich, 1992; Van Enckevort and van der Berg, 1998). More importantly, impurity effects on calcite have been shown to be highly direction-specific (Paquette and Reeder, 1995; Reeder, 1996; Astilleros et al., 2000; Davis et al., 2000; Lea et al., 2001; Astilleros et al., 2002). In addition, impurities such as Mg and Ba can selectively produce roughened or ragged step edges (Astilleros et al., 2000; Davis et al., 2000). In our earlier

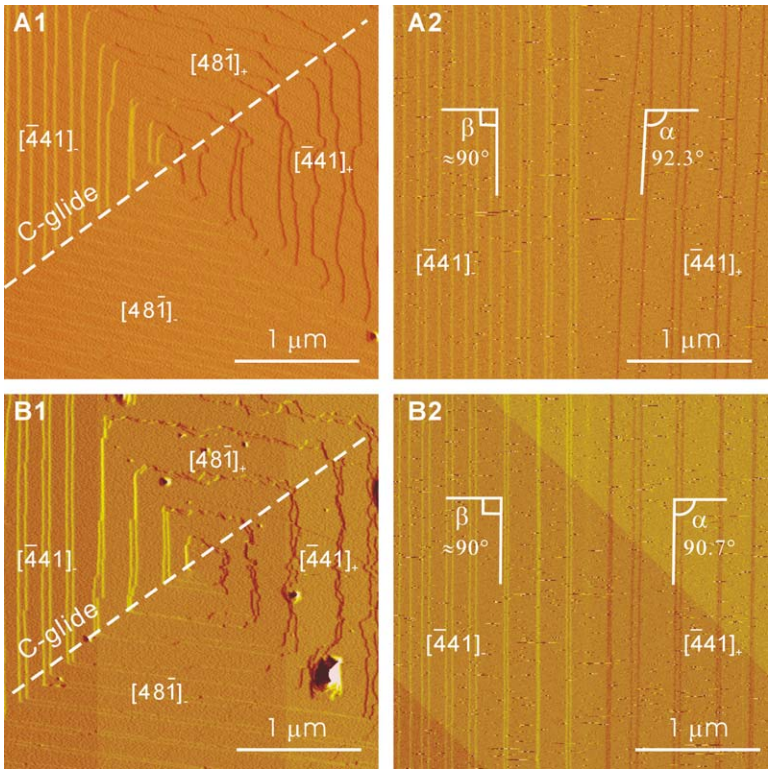

Fig. 7. Crystallographic direction specific behavior of the $\langle\bar{4}41\rangle_+$ and $\langle\bar{4}41\rangle_-$ steps in solutions with IAP $= 10^{-8.47}$ shown in AFM images with (A1 and B1) full scan and (A2 and B2) the slow scan axis disabled. Notice that $\alpha > 90°$ and $\beta \approx 90°$, indicating the $\langle\bar{4}41\rangle_+$ steps are retreating (i.e., dissolving) while the $\langle\bar{4}41\rangle_-$ steps stand still.

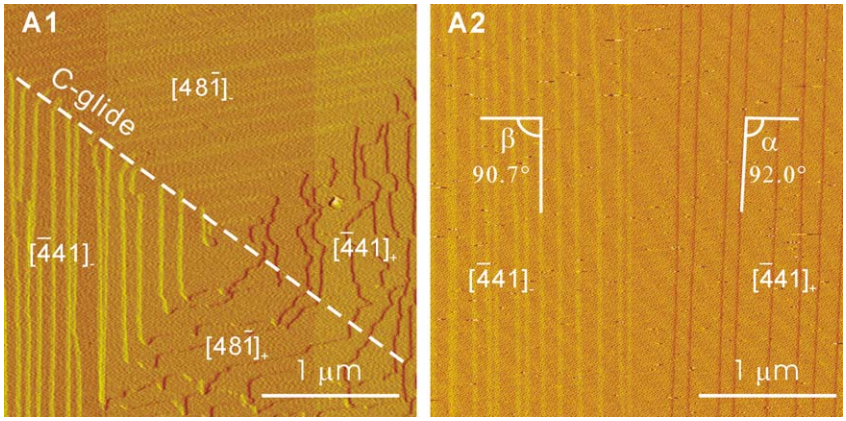

Fig. 8. Crystallographic direction specific behavior of the $\langle\bar{4}41\rangle_+$ and $\langle\bar{4}41\rangle_-$ steps in solutions with IAP $= 10^{-8.51}$ shown in AFM images with (A1) full scan and (A2) the slow scan axis disabled. Notice that both α and β are now greater than 90°, indicating the and $\langle\bar{4}41\rangle_+$ and $\langle\bar{4}41\rangle_-$ steps are moving in the same direction: both sets of steps are dissolving.

study (Teng et al., 1999), we reported the development of ragged positive steps and reversed hillock morphology on calcite $\{10\bar{1}4\}$ faces at near equilibrium conditions and concluded that the observations were due to the effect of impurities from the lower grade reagents used in the experiments. These findings strongly suggest that the influence of impurities should not be discounted when interpreting the present observations.

Three lines of evidence may argue that impurity effects are probably insignificant in relation to the phenomena observed in this study. First, in contrast to previous studies that focused on the effects of impurities, our experiments were conducted at a much lower impurity levels (Tables 1 and 2). In Teng et al. (1999), the impurity concentrations in the experimental solutions were high due to the use of a 0.1 M NaCl (made from 99% NaCl reagent) solution as a background electrolyte. In the present study, all reagents were of high purity (i.e. >99.99%) and no salt was used to adjust the ionic strength ($\sim 10^{-3}$ M on average). ICP analyses (Table 1) of the reagents used in this study not only

Table 1
ICP analysis of impurity concentrations (ppm) in the reagents used in this study

	Mg	Ca	K	Sr	Ba	Fe	Bi	Mn	Si	B	S
$NaHCO_3$	8.3	35		0.1	0.5	0.5		0.1	2.0	0.2	20
$CaCl_2 \cdot 2H_2O$	9.2		12.9	129	7.5		12.1		0.3		

Table 2
Concentrations of major impurities (mol/l) in this study and their threshold values[a] as well as directional affinity[b] for calcite

	$C_{cur.\ conc.}$	Threshold values	Directional affinity[b]
Mg	10^{-7}	10^{-5}	Negative steps
Ba	10^{-7}	10^{-3}	Positive steps
Sr	10^{-6}	10^{-5}	Positive steps

[a] See text for detailed citations.
[b] Preferred direction for ion incorporation.

show a lower concentration of total impurities, but detect no P and less Fe ($\sim 10^{-9}$ mol/l) than the reagents used in the earlier study (Teng et al., 1999).

Second, for impurities to have significant impact on calcite precipitation and dissolution, their concentrations must be higher than certain threshold values (Meyer, 1984). Furthermore, it appears that the magnitude of these thresholds is not saturation dependent even though it was suggested that the effectiveness of impurities as inhibitors increases as equilibrium is approached. For example, Sjöberg (1978) reported that, as the saturation state of the parent solution approached equilibrium, the inhibition of calcite dissolution by magnesium becomes increasingly effective but only at a magnesium concentration greater than 10^{-3} mol/l. Similar observations were documented by Sabbides and Koutsoukos (1995), who conducted calcite dissolution experiments in the presence of Mg at near equilibrium conditions (i.e., $\Omega = 0.924$–0.847) but did not observe a reduction in the dissolution rate until the Mg^{2+} concentration was increased to $\sim 10^{-5}$ mol/l. Further, Gutjahr et al. (1996) reported no inhibition of calcite dissolution rate by magnesium at a saturation state of $\Omega \sim 0.755$ when the concentration of Mg was less than 3×10^{-4} mol/l. In this study, the concentrations of common divalent cations Mg^{2+}, Ba^{2+}, and Sr^{2+} ranged from $\sim 10^{-6}$ to $\sim 10^{-7}$ mol/l (Table 1) and were one to four orders of magnitude lower than the corresponding threshold values (Table 2) reported in the literature (Meyer, 1984; Astilleros et al., 2000; Davis et al., 2000; Lea et al., 2001).

The third argument concerns the impurity contribution from the seed crystals. It is conceivable that the dissolution of the Iceland spar used in the AFM experiments released impurities to the solutions. Nevertheless, we believe that our experimental design minimizes this possibility. As noted in Section 3, the AFM experiments were not conducted directly on the cleavage surfaces of the seed crystals but on steps that had grown from our experimental solutions. The growth hillocks where the new steps emerged were allowed to grow for 3–4 h before imaging was carried out. Hence, the near-equilibrium dissolution, observed during data collection, should occur on the newly grown steps without a significant contribution of the original seed crystals. On a few occasions, when deep etch pits developed on the spirals (Fig. 7), impurities of the Iceland spar would have been released. Nonetheless, their contributions should be trivial given the small size of the pits. Finally, the slow dissolution rates at near equilibrium conditions and the relative short residence time of the solutions in the fluid cell ($\sim$2.4 s), during data collection, should have prevented significant accumulation of impurities in the reaction chamber.

5.2. Size effect on solubility

As predicted by Eq. (4c), the measured critical step lengths on growth spirals (equivalent to the sizes of critical nuclei, see Burton et al., 1951) scale inversely to the saturation states (Fig. 4). More importantly, the theoretical dependence of K_b/K_{sp} upon crystal size, Eq. (4d), calculated by using $\bar{\gamma} = 0.33 J/m^2$ (de Leeuw, 2002), $\tau = 6.135$ (assuming a rhombohedral growth unit), and $\rho = 2.71$ g/cm^3 shows a good agreement with the experimental measurements. The results illustrate that while the deviation of K_{sp} from K_b increases very rapidly with decreasing step lengths below a few 100 nm, the influence of crystal size diminishes slowly when step lengths are beyond the micrometer scale (inset in Fig. 4). For example, the difference between K_b and K_{sp} reduces from $\sim$5% to $\sim$2% when the step length increases from approximately 1 μm to 3 μm.

5.3. Direction effect on solubility

Geometrically, the difference between the positive and the negative steps (Fig. 1) lies in the angles formed by the step risers and the terraces. Structurally, the difference stems from the change in orientation of the carbonate groups. In contrast to these geometric and structural differences and the resulting energetic distinction between the two sets of steps (de Leeuw et al., 1999; Duckworth et al., 2004), the surface area change associated with the attachment of each $CaCO_3$ molecule is identical at the positive and negative edges because the step height and the separation between the calcium and carbonate ions are the same in both directions (Paquette and Reeder, 1995). Incorporating such information into the P × N model (directly applicable to calcite) and Eqs. (7a and 7b) in Section 2.2, we find that $K_{b,+}$ (solubility at the positive steps) and $K_{b,-}$ (solubility at the negative steps) will inherently be different for calcite: while dA_+, dA_-, dn_+, and dn_- are identical for positive and negative steps and hence do not

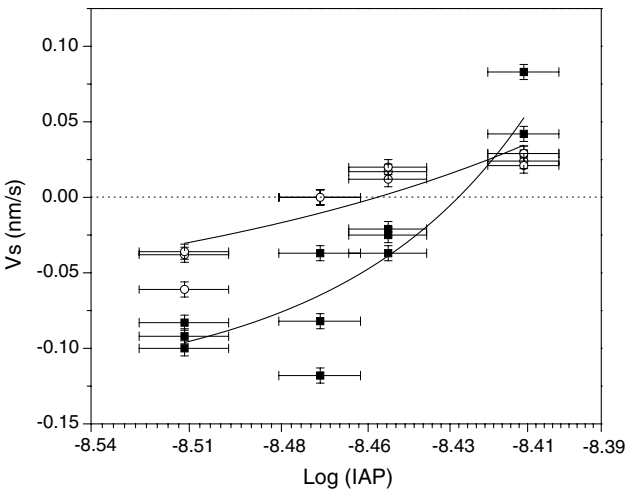

Fig. 9. Experimental measurements of step velocity vs. log (IAP) of the input solutions. Positive and negative velocities represent step advance and retreat, respectively. Note that in the range of log (IAP) $\approx (8.41 \sim 8.45)$ to 8.47, retreat in the $\langle \bar{4}41 \rangle_+$ direction (■) and advance in the $\langle \bar{4}41 \rangle_-$ direction (○) occur simultaneously.

have direction dependence, $\gamma_{+,+}$ and $\gamma_{-,-}$ are not equivalent because they are related to different bonding environments on calcite surfaces, leading to the conclusion that the two sets of steps have different solubilities.

The prediction appears to be consistent with the experimental observations. The results presented here suggest that solutions are supersaturated with respect to both the positive and negative steps when the IAP value is greater than $10^{-8.41}$. On the other hand, solutions become undersaturated with respect to the positive steps while remaining supersaturated with respect to the negative steps when $(10^{-8.41} \sim 10^{-8.45}) > \mathrm{IAP} > 10^{-8.47}$. A complete undersaturation with respect to all $\langle \bar{4}41 \rangle$ steps is only achieved when the IAP of the solutions falls below $10^{-8.51}$ (Fig. 9). The greater solubility of the positive steps is also consistent with their larger step energies (Teng et al., 1998).

6. Concluding remark

Theoretical and experimental arguments are presented to illustrate the difference and the relationship between crystal solubility and solubility product. Equilibrium thermodynamics suggests that the solubility K_b is always greater than the solubility product K_{sp}, but the difference is grain size dependent: whereas K_b deviates sharply from K_{sp} as crystal size decreases, the solubility slowly approaches the solubility product when crystals are larger than a few micrometers. In addition, thermodynamic considerations indicate that K_b is face dependent as long as energy change associated with the attachment of individual growth units in symmetrically unrelated directions is nonequivalent. In agreement with these predictions, AFM measurements of critical step lengths on calcite $\{10\bar{1}4\}$ cleavage faces show a clearly defined inverse dependence on saturation state that closely follows the theoretical curve. Furthermore, simultaneous retreat and advance are observed at the $\langle \bar{4}41 \rangle_+$ and $\langle \bar{4}41 \rangle_-$ steps, respectively, in a narrow range of saturation near equilibrium conditions, indicating that steps in those two directions may have different solubilities.

These findings suggest that whereas it is reasonable to approximate the solubility, K_b, by K_{sp} when crystals are large, the size-dependence of K_b should not be ignored when nano- to submicron-sized crystals are concerned. Moreover, the direction-dependence of K_b should be taken into account if the thermodynamic and kinetic properties of monolayer steps are of interest. For the dissolution and growth of large crystals, it is not necessary to invoke the direction-dependence of K_b. Nevertheless, it is important to understand that surface properties such as step velocity and morphology are directly related to the direction-dependence of K_b, especially at near equilibrium conditions.

Acknowledgments

We thank Carlos M. Pina, Jeanne Paquette, and one anonymous reviewer for helpful and constructive comments and suggestions during review. We also thank Alfonso Mucci for revisions and corrections that improved the writing of this manuscript during the final editorial handling. This work was supported by the office of Basic Energy Science, US DOE, through Grant No. DE-FG02-02ER15366, and the Chinese NSF Joint Research Fund for Overseas Young Scholars through Grant No. 40428004.

Associate editor: Alfonso Mucci

References

Allison, J.D., Brown, D.S., Nove-Gradac, K.J., 1991. MINTEQA2/PRODEFA2, A geochemical assessment model for environmental systems: Version 3.0 User's Manual, US Environmental Protection Agency, Athens, GA.

Astilleros, J.M., Pina, C.M., Fernández-Díaz, L., Putnis, A., 2000. The effect of barium on calcite $\{10\bar{1}4\}$ surfaces during growth. *Geochim. Cosmochim. Acta* **64**, 2965–2972.

Astilleros, J.M., Pina, C.M., Fernández-Díaz, L., Putnis, A., 2002. Molecular-scale surface processes during the growth of calcite in the presence of manganese. *Geochim. Cosmochim. Acta* **66**, 3177–3189.

Burton, W.K., Cabrera, N., Frank, F.C., 1951. The growth of crystals and the equilibrium structure of their surfaces. *Royal Soc. London Philos. Trans.* **A243**, 299–358.

Cabrera, N., Vermilyea, D.A., 1958. The growth of crystals from solution. In: Doremus, R.H., Roberts, B.W., Turnbull, D. (Eds.), *Growth and Perfection of Crystals*. John Wiley & Sons, London, pp. 393–410.

Che, J.G., Chan, C.T., Jian, W.E., Leung, T.C., 1998. Surface atomic structures, surface energies, and equilibrium crystal shape of molybdenum. *Phys. Rev. B* **57**, 1875–1880.

Davis, K.J., Dove, P.M., De Yoreo, J.J., 2000. The role of Mg^{2+} as an impurity in calcite growth. *Science* **290**, 1134–1137.

de Leeuw, N.H., Parker, S.C., Harding, J.H., 1999. Molecular dynamics simulation of crystal dissolution from calcite steps. *Phys. Rev. B* **60**, 13792–13799.

de Leeuw, N.H., 2002. Surface structures, stabilities, and growth of magnesian calcites: a computational investigation from the perspective of dolomite formation. *Am. Mineral.* **87**, 679–689.

Duckworth, O.W., Cygan, R.T., Martin, S.T., 2004. Linear free energy relationships between dissolution rates and molecular modeling energies of rhombohedral carbonates. *Langmuir* **20**, 2938–2946.

Enüstün, B.V., Turkevich, J., 1960. Solubility of fine particles of Strontium sulfate. *J. Am. Chem. Soc.* **82**, 4502–4509.

Gibbs, J.W., 1961. *The Scientific Papers of J. Willard Gibbs*, vol. I. Dover Publications, New York.

Gutjahr, A., Dabringhaus, H., Lacmann, R., 1996. Studies of the growth and dissolution kinetics of the $CaCO_3$ polymorphs calcite and aragonite: II. The influence of divalent cation additives on the growth and dissolution rates. *J. Cryst. Growth* **158**, 310–315.

Jensen, D.L., Boddum, J.K., Tjell, J.C., Christensen, T.H., 2002. The solubility of rhodochrosite ($MnCO_3$) and siderite ($FeCO_3$) in anaerobic aquatic environments. *Appl. Geochem.* **17**, 503–511.

Land, T.A., De Yoreo, J.J., Lee, J.D., 1997. An in-situ AFM investigation of Canavalin crystallization kinetics. *Surf. Sci.* **384**, 136–155.

Lea, A.S., Amonette, J.E., Baer, D.R., Liang, Y., Colton, N.G., 2001. Microscopic effects of carbonate, manganese, and strontium ions on calcite dissolution. *Geochim. Cosmochim. Acta* **65**, 369–379.

Meyer, H.J., 1984. The influence of impurities on the growth rate of calcite. *J. Cryst. Growth* **66**, 639–646.

Nernst, H.W., 1889. Über gegenseitige beeinflussung der löslichkeit von salzen. *Z. Physik. Chem* **4**, 372–381.

Paquette, J., Reeder, R.J., 1995. Relationship between surface structure, growth mechanism, and trace element incorporation in calcite. *Geochim. Cosmochim. Acta* **59**, 735–751.

Park, N.S., Kim, M.W., Langford, S.C., Dickinson, J.T., 1996. Atomic layer wear of single-crystal calcite in aqueous solution using scanning force microscopy. *J. Appl. Phys.* **80**, 2680–2686.

Parks, G.A., 1990. Surface energy and adsorption at mineral/water interfaces: an introduction. In: Hochella, M.F., White, A.F. (Eds.), *Mineral–Water Interface Geochemistry, Reviews in Mineralogy*. Mineralogical Society of America, pp. 133–175.

Plummer, L.N., Busenberg, E., 1982. The solubilities of calcite, aragonite and vaterite in CO_2–H_2O solutions between 0 and 90 °C, and an evaluation of the aqueous model for the system $CaCO_3$–CO_2–H_2O. *Geochim. Cosmochim. Acta* **46**, 1011–1040.

Reeder, R.J., 1996. Interaction of divalent cobalt, zinc, cadmium, and barium with the calcite surface during layer growth. *Geochim. Cosmochim. Acta* **60**, 1543–1552.

Sabbides, G., Koutsoukos, P.G., 1995. Dissolution of calcite carbonate in the presence of magnesium and orthophosphate. In: Amjad, Z. (Ed.), *Mineral Scale Formation and Inhibition*. Plenum Press, New York, pp. 73–86.

Simon, B., Boistelle, R., 1981. Crystal growth from low temperature solutions. *J. Cryst. Growth* **52**, 779–788.

Sjöberg, E.L., 1978. Kinetics and mechanism of calcite dissolution in aqueous solutions at low temperatures. *Stockholm Contributions in Geology* **32**, 92.

Smith, R.W., Hem, J.D., 1972. Effect of aging on aluminum hydroxide complexes in dilute aqueous solutions. *U.S. Geological Survey Water-Supply Paper*, 1827D.

Stieglitz, J., 1908. Note on the solubility product. *J. Am. Chem. Soc.* **30** (6), 946–954.

Teng, H.H., Dove, P.M., Orme, C.A., De Yoreo, J.J., 1998. The thermodynamics of calcite growth: a baseline for understanding biomineral formation. *Science* **282**, 724–727.

Teng, H.H., Dove, P.M., De Yoreo, J.J., 1999. Reversed calcite morphologies induced by microscopic growth kinetics: insight into biomineralization. *Geochim. Cosmochim. Acta* **63**, 2507–2512.

Teng, H.H., Dove, P.M., De Yoreo, J.J., 2000. Kinetics of calcite growth: surface processes and relationships to macroscopic rate laws. *Geochim. Cosmochim. Acta* **64**, 2255–2266.

Teng, H.H., 2005. AFM measurement of step kinetics for the growth and dissolution of crystallites. *Spectroscopy* **20** (6), 16–20.

Van Enckevort, W.J.P., van der Berg, A.C.J.F., 1998. Impurity blocking of crystal growth: a Monte Carlo study. *J. Cryst. Growth* **183**, 441–445.

Voronkov, V.V., Rashkovich, L.N., 1992. Influence of a mobile adsorbed impurity on the motion of steps. *Sov. Phys. Crystallogr.* **37** (3), 289–295.